Method for the generation and visualization of cross-sectional images of three-dimensional point spread functions for rotationally symmetric intraocular lenses

JAN SIEVERS,[1,2,3] RICARDO ELSNER,[1,2] SEBASTIAN BOHN,[1,2] MELANIE SCHÜNEMANN,[1,2] HEINRICH STOLZ,[2,4] RUDOLF F. GUTHOFF,[1,2] OLIVER STACHS,[1,2] AND KARSTEN SPERLICH[1,2,*]

[1]*Department of Ophthalmology, Rostock University Medical Center, 18057 Rostock, Germany*
[2]*Department Life, Light & Matter, University of Rostock, 18055 Rostock, Germany*
[3]*Institute of Physics, Martin–Luther–University Halle–Wittenberg, 06120 Halle (Saale), Germany*
[4]*Institute of Physics, University of Rostock, 18055 Rostock, Germany*
[*]*karsten.sperlich@uni-rostock.de*

Abstract: Cross-sectional images of three-dimensional point spread functions of intraocular lenses are used to study their image formation. To obtain those, light sheet-based methods are established. Due to the non-negligible thicknesses of the light sheets, the image quality of the cross-sectional images is constrained. To overcome this hurdle, we present a dedicated evaluation algorithm to increase image quality in the post-processing step. Additionally, we compare the developed- with the light sheet method based on our own investigations of a multifocal diffractive intraocular lens conducted in an in-house designed optical bench. The comparative study showed the clear superiority of the newly developed method in terms of image quality, fine structure visibility, and signal-to-noise ratio compared to the light sheet based method. However, since the algorithm assumes a rotationally symmetrical point spread function, it is only suitable for all rotationally symmetrical lenses.

1. Introduction

During cataract surgery, the natural eye lens is removed and replaced by an intraocular lens (IOL). The simplest IOL is a monofocal lens [1]. In this case, patients can only see sharp at one distance and need visual aids for other distances. Multifocal IOLs (MIOLs), among others, provide independence from visual aids. These have two or more focal points [2]. Multifocality of IOLs is realized by principles of refraction, diffraction, or a combination of both [3–5].

To verify the manufacturers' data and to compare the optical properties of IOLs with each other, experimental determination of these properties is essential. For this reason, it is an important part of preclinical IOL testing.

Simpson used the EROS solid state MTF equipment (formerly Ealing Electro-Optics, now Coherent, Santa Clara, USA) to capture the line spread functions and calculate the corresponding modulation transfer functions (MTFs) using the Fourier transform [6]. Carretero et al. as well as Bos et al. developed interferometric approaches based on an optical bench design to analyze optical properties of IOLs. [7,8]. Ravalico et al. presented one of the first in-house optical benches for capturing 2D-PSF images at the focal points of several IOLs and computed the energy efficiency [9]. All of these early stage optical benches had the similar characteristics of the nowadays used optical benches like a collimated beam of light source, IOL stored in a model eye, camera for data acquisition and computer for data processing, but each setup with different specifications and parameters and hence impeding direct comparisons of these early results.

To ensure comparability of the optical IOL properties, the ISO standard 11979-2:2000-07 [10] was established in the year 2000 recommending the use of an optical bench with special technical specifications as the experimental setup for IOL examinations. Since its establishment, most papers on the research of optical properties of IOLs focus on the determination of MTFs and through-focus MTFs using optical benches, e.g. [11–15].

Generally, such a setup allows recording the 3D light distribution caused through the investigated IOL by moving a microscope camera unit along the optical axis capturing images of the 2D point spread function (2D-PSF) of the IOL at different axial positions. By lining up all the images of a captured image stack to a 3D image, the light distribution inside the volume corresponds to the 3D point spread function (3D-PSF) of the investigated IOL. Using this technique, Millán et al. captured the 3D-PSFs of three MIOLs to study the through-focus energy efficiency and longitudinal chromatic aberration [16]. Another important IOL property which can be calculated from a captured 3D-PSF is the cross-sectional image (CSI). It is thus determined by cutting out a thin volume of the captured 3D-PSF along the optical axis and averaging the lateral intensity distribution line by line. To the best of our knowlede, Petelczyc et al. used this technique for the first time to calculate the CSIs of six selected MIOLs using data captured with an in-house optical bench [17].

Another approach to acquire CSIs of IOLs is the application of a fluorescein bath, which is described in detail in [18]. A thin light sheet illuminates an IOL placed in a fluorescein bath. The light distribution occurring behind the IOL becomes visible due to the fluorescence of the excited fluorescein. Light emitted laterally to the optical axis of the system, due to fluorescence and scattering, is captured by a camera mounted perpendicular to the resulting CSI. Due to the finite width of the light sheet, the fluorescein molecules are stimulated within a volume along the optical axis. Thus, the cross-sectional image captured by the camera equals the averaged intensity distribution of the illuminated volume. The use of scattering particles like Ouzo or milk powder is possible as well and offers an alternative to the fluorescein molecules [19,20].

The CSIs acquisition and analysis of IOLs is a well-established component of preclinical IOL examinations [21]. These profiles are used to study the experimental image formation created by the investigated IOL [22]. Further, important parameters such as through-focus curves, MTFs, lateral intensity distributions and add powers of MIOLs can be derived from CSIs [19,20,23,24].

Both methods are light sheet-based and the standard for the determination of cross-sectional images in this field of research but the thickness of the light sheet in the case of the fluorescein bath or the width of the extracted volume in the case of the optical bench always results in an image quality decrease of the investigated cross-sectional images.

Many IOLs have a rotationally symmetric design, a fact, that we exploit to increase the image quality and signal-to-noise ratio. In this work, we use an in-house designed optical bench for the automatic acquisition of 3D-PSFs at various pupil sizes for a trifocal diffractive AT LISA tri 839MP (Carl Zeiss Meditec AG, Jena, Germany). In addition, we present a proprietary algorithm for exploiting the rotational symmetry. The new algorithm was applied to the obtained 3D-PSFs to determine the CSIs and subsequently compared with the standard, light sheet-based methods in terms of their image qualities, signal-to-noise ratios, and fine feature visibilities.

2. Methods

2.1. Experimental setup

Our in-house designed optical bench is based on the ISO 11979-2:2014-12 standard [25] and the documented optical benches of other working groups investigating imaging properties of IOLs [17,26,27]. Figure 1 shows the schematic illustration of the experimental setup for obtaining the IOL light distribution. The green LED light with a central wavelength $\lambda = 530$ nm and a FWHM $= 47$ nm passes a pinhole (10 μm, Thorlabs, Newton, New Jersey, USA) and is collimated by an achromatic lens (f $= 150$ mm, AC254-150-A1, Thorlabs, Newton, New Jersey, USA). The

diameter of the parallel beam can be changed by an aperture (SM1D12C, Thorlabs, Newton, New Jersey, USA). The model eye was originally designed for the VirtIOL (10Lens S.L.U., Terrassa, Spain) device, which is a see-through device for the simulated implantation of IOLs [28–30].
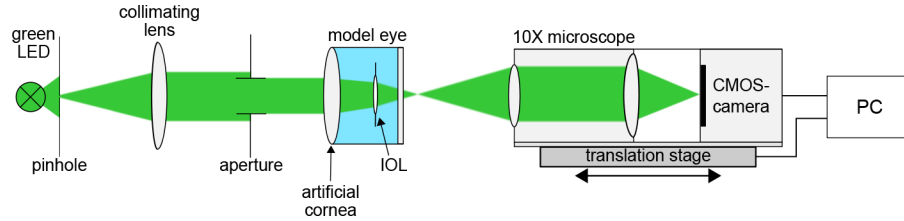

Fig. 1. Schematic illustration of the optical bench for the measurement of the 3D-PSF of the investigated IOL.

It consists of an achromatic lens (f = 40 mm) as an artificial cornea on the front side, a glass window on the backside, and an IOL holder in between. The medium inside the model eye is distilled water. Simulations with the ray-tracing software FRED Optical Engineering Software 18.61.2 (Photon Engineering, Tucson, Arizona, USA) showed a linear dependency between the aperture diameter d_A and the illuminated diameter of the IOL d_{IOL}:

$$d_{IOL} = 0.978 \cdot d_A \tag{1}$$

The scaling factor depends on the focal length and the distance between model cornea and IOL. This distance was in our case about ≈ 2.1 mm. Behind the model eye, a microscope objective (IC-10 MD-Plan, NA = 0.25, Olympus, Shinjuku, Japan) and a 12-Bit monochrome CMOS-camera (UE-3880CP-M-GL, IDS Imaging Development Systems GmbH, Obersulm, Germany) with an image resolution of 3088 × 2076 pixels and a pixel size of 2.4 µm are attached to a translation stage which can be moved along the optical axis. Further, the translation stage is motorized using a NSC200-Controller and a TRA25PPM actuator (both Newport Corporation, Irvine, California, USA). The camera and the translation stage are both controlled by a dedicated script in LabVIEW 2019 SP1 (National Instruments Corporation, Austin, Texas, USA). Accordingly, multiple images of the IOL light distribution can be captured automatically for different axial positions. For the presented experiments, the total travel distance of the translation stage $s = 1.91$ mm with an increment $\Delta s = 7.63$ µm is used. Hence, a stack of images includes 251 images. For each position, the light distribution and the background signal are captured multiple times.

2.2. Proprietary algorithm for cross-sectional image determination

A proprietary algorithm, written in Mathematica 12.0 (The Wolfram Centre, Oxfordshire, United Kingdom), was used for automated analysis of the captured 3D-PSF. Considering the fact, that the surface of the investigated diffractive MIOL is rotationally symmetric and consequently the 3D-PSF too, an annulus integration method can be applied. In short, the general procedure is as follows. Each camera image is divided into a small central disk surrounded by thin annuli with a specific width. Afterward, the intensity in each zone is summed up, the background is estimated by a linear fit and subtracted (cf. Fig. 2(a)). In the next step, this noise corrected intensity profile is divided by its area (cf. Fig. 2(b)), resulting in an array of intensity values from the center to the edge for each axial position. These arrays are then merged to form an image that, together with its mirror image on the optical axis, produces the averaged cross-sectional image of the 3D PSF. In the following, we will explain this procedure in more detail and how to circumvent the aforementioned decrease in image resolution.

For each axial position, the averaged 12-bit camera images and the corresponding averaged background images are imported and subtracted. Negative pixel values are replaced by their
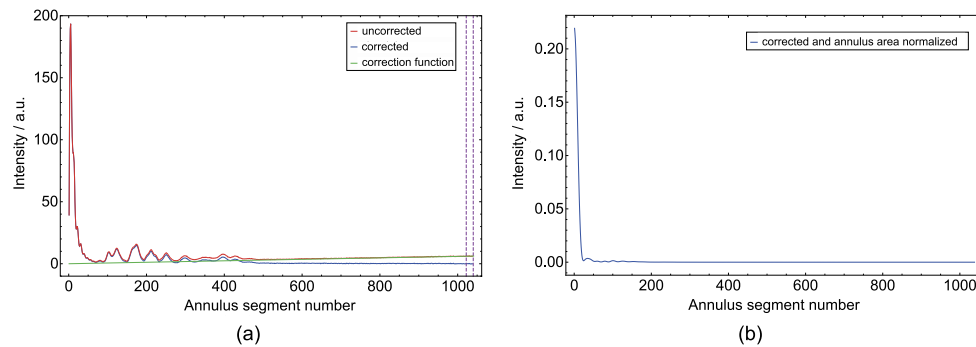
Fig. 2. (a) Exemplary explanation of the noise correction by a linear correction function. Due to the linear area growth of the annuli and high gray values of the focal point area comparing to the outer image regions. The peak of the shown intensity profile is not located in the origin. (b) The noise corrected and annulus segment area normalized intensity course as a function of the annulus segment number. The central peak is located in the origin.

absolute values. To ensure that the intensity distributions are not shifted with respect to the concentric rings, the light distribution of each image is centered on the center point of the image. The annulus integration method is realized using an annuli mask. This one is determined by dividing the image for the used image resolution into a central disk and surrounding concentric circular rings with a constant width of 4 px. The pixel positions of the disk and each annulus are classified and saved in the file of the annuli mask which has to be calculated only once since the image resolution remains the same during the experiments. However, due to the specific width of each circular ring, the final cross-sectional image resolution is decreased in one dimension. To circumvent the decrease, the corrected images are upsampled by a factor of four using cubic spline interpolation (Mathematica function `IMAGERESIZE` with the method "Cubic"). With the annuli mask, the pixel classified to one of the concentric rings can be extracted for each enlarged image of an image stack (Mathematica function `EXTRACT`). Further, the intensity of each concentric ring is calculated by adding up the intensities of the corresponding pixels. Thus, the intensity distribution of each image is represented as an intensity function depending on the concentric rings.

Due to the constant radius, the area of the concentric rings increases linearly from the center outward to the periphery of the image. The noise term of the intensity signal thus increases linearly from the center outwards. This noise signal, occurring in each of the new intensity distributions of the images, is canceled out by a linear correction function and shown exemplarily in Fig. 2(a). The uncorrected intensity curve, shown as –, and the corrected intensity curve, shown as –, are presented as a function of the annulus segment number. The slope of the noise correction function, illustrated as –, is determined by the intensity values of the 20 highest annulus segment numbers, illustrated as --, and the fact that the correction function has to pass through the coordinate origin. Notice, the peak of the shown intensity as a function of the annulus segment number is not located at segment number = 0, due to the linear area growth of the annulus and high gray values of the focal point comparing to the outer image regions. The corrected intensity curves are normalized to the various annulus segment areas that shifts the peak position to the segment number = 0.

In the next step, the corrected and area-normalized 1D-intensity profiles of each image (see. Fig. 2(b)) are lined up, mirrored, and presented as an overview graphic in intensity-dependent gray values, which is the cross-sectional image of the investigated intraocular lens. A cross-sectional profiles calculated with the new annulus integration method is referred to as rotationally averaged cross-sectional image (RA-CSI) in the following.

The highly parallelized Mathematica algorithm needs still $\approx 40\,\text{min}$ for the complete evaluation of an image stack with 251 images using a workstation equipped with an AMD Ryzen 9 3950X processor with 16 cores at 3.493 GHz (AMD, Santa Clara, USA) and 32 GB RAM.

Throughout the rest of the manuscript, this proprietary algorithm is referred to as new algorithm.

2.3. *Signal-to-noise ratio*

The signal-to-noise ratio (SNR) is generally defined as the ratio of the averaged signal amplitude divided by the noise variance. This metric is used to determine the quality of measured signals. The higher the SNR value the better the quality of the measured signal. Depending on the field of application, modifications of the general definition of SNR exist.

In this paper, the SNR is defined as:

$$\text{SNR} = \frac{(A_\text{S} - A_\text{N})}{\sigma_\text{N}}, \tag{2}$$

where A_S and A_N are the averaged amplitude pf the captured signal and noise, respectively, and σ_N denotes the variance of the noise [31,32]. The amplitude of the signal A_S is calculated by the 16 pixels around the center point of each 2D-PSF image. The variance σ_N and the amplitude A_N of the noise, respectively, are determined from four 2×2 pixels squares, one of which is located in each corner of the respective 2D-PSF image.

2.4. *IOL and measurement specifications*

The IOL under investigation is a diffractive trifocal AT LISA tri 839MP (Carl Zeiss Meditec AG, Jena, Germany) with a base optical power for the far focus of 22.5 dpt with +3.33 dpt and +1.66 dpt add powers for the near and the intermediate foci respectively.

Image stacks of the 3D-PSFs were measured for the value d_IOL from 2.5 mm to 6.0 mm in 0.5 mm steps. For each axial position of the image stacks, six single images were captured of the 2D-PSF and the background signal, respectively. The obtained 3D-PSFs were evaluated with the previously explained algorithm.

3. Results

3.1. *Influence of the light sheet width on the cross-sectional image*

An image stack with six images and six background images for each axial position in a 12-Bit format was captured using the presented optical bench for an aperture d_A of 3 mm. This pupil diameter is prescribed by ISO standard 11979-2 [25] for the investigation of IOLs and has its origin in the reduced pupil diameter according to the average age of cataract patients under photopic conditions [33,34]. By using the first part of the new algorithm, the different centered and background signal corrected 3D-PSFs were determined.

In analogy to the light sheet-based method, the cross-sectional image of the 3D-PSF was determined by extracting a narrow volume consisting of 15, 150, 1500 pixels, respectively, of the averaged and background corrected images of the image stack. Those specific pixel ranges were chosen for the following reasons, starting with the last one mentioned.

Peteclczyc et al. used an optical bench for recording 3D-PSFs of several MIOLs. Further, they reported that "··· Figure 4 shows Through-Focus PSFs (TF PSFs) composed of perpendicular projections of all 101 PSFs, obtained for successive defocus values in the linear light intensity scale. Each projection was created by calculating the cumulated intensities of every cross-section of the PSF along the horizontal axis. ..." [17]. Accordingly, we present also a horizontal projection cross-sectional image (P-CSI) with a reduced width of 1500 pixels. In the case of using a fluorescein bath, the investigated IOL is illuminated by a light sheet. Reiß et al. used a light sheet with 0.35 mm [18] and Eppig et al. a light sheet with a width of 0.3 mm [20]. For

the used optical components and the investigated trifocal MIOL, the latter width corresponds on average of the three widths of the focal points to a sensor width of 159 pixels and the first one to a sensor width of 136 pixels. Accordingly, those two widths of the light sheets match on medium to a sensor width of ≈ 150 pixels. Furthermore, the CSI is shown for a width of 15 pixels to investigate the intensity of the wave propagation in a thin volume along the optical axis. The selected light sheet widths on the sensor of 15, 150, and 1500 pixels correspond to a light sheet thicknesses t of 4.3, 43, and 430 µm, respectively.

Fig. 3 shows these cross-sectional images in intensity-dependent gray values with (left side) linearly and (right side) logarithmically scaled intensities due to the linearity of the camera sensor and the logarithmic visual perception of the human eye [35,36]. The lateral image areas of the shown CSI, perpendicular to the axial position, are trimmed and stretched linearly to three times the width of the original to improve the visibility of the separate light rays. Further, each of the CSIs is scaled to its maximum intensity value. The near focus is at an axial position of ≈ 0.3 mm, the intermediate focus at ≈ 0.9 mm and the far focus at ≈ 1.35 mm. First, we will take a closer look at the linear scaled CSIs. The CSI of 4.3 µm width shows the three focal points, which are clearly spatially separated from each other, as well as ray extensions at the outer focal areas along the optical axis. As the thickness of the investigated volume increases, it can be observed that the spatial separation between the focal points blurs, especially for the separation of intermediate and far focus and the ray extensions at the outer focus areas become more visible. In addition, more structures appear in the vicinity of the optical axis. These are especially present around the intermediate focus and can be attributed to halos which are generated at each focal point by the out-of-focus energy of other focal points [37] and lead generally to a reduction of visual acuity at the specific distance [38].
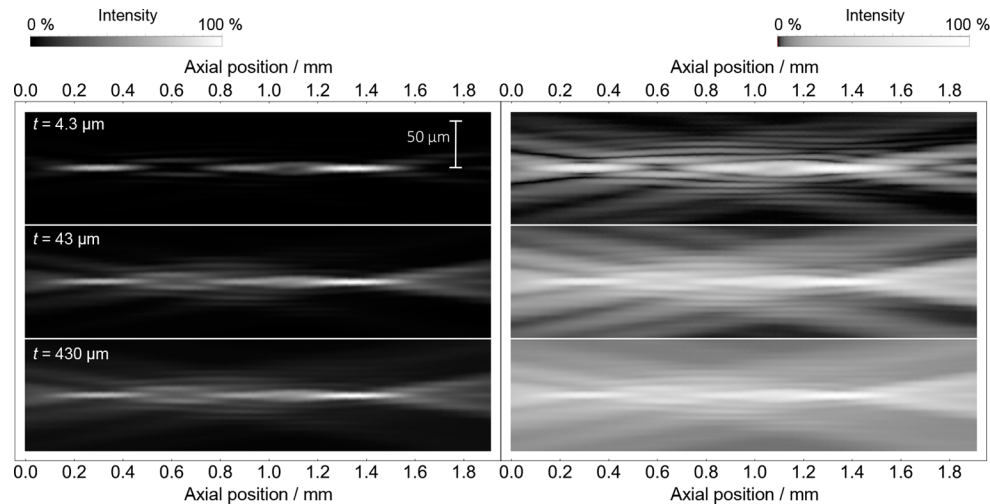

Fig. 3. Influence of the different light sheet width t on the cross-sectional image of the investigated trifocal IOL in intensity-dependent gray values with (left) linearly- and (right) logarithmically scaled intensities for an illuminated IOL-diameter $d_{IOL} = 2.93$ mm. The near focus is at an axial position of ≈ 0.3 mm, the intermediate focus at ≈ 0.9 mm and the far focus at ≈ 1.35 mm.

Due to the logarithmic visual sensitivity of the eye [39] and the lack of possibilities to present high dynamic range content on low dynamic range media, the CSIs just presented are also shown in logarithmically scaled intensities on the right side of Fig. 3. The comparison of the linearly and logarithmically scaled CSIs averaged over 4.3 µm shows that the transition of the intermediate and far focus is fluent in the logarithmically scaled illustration but fine structures of low intensity

appear over the whole image area. In addition to the three focal points, another focal point appears in this illustration at an axial distance of 1.9 mm. Assuming positive diffraction order numbers for the wanted diffraction orders, this focal point may be attributed to a negative diffraction order [40,41]. Starting from the optical axis, there are alternating bright and dark stripes in the lateral image areas, which are due to interference effects between the individual light beams from the different zones of the MIOL. Fine structure visibility terms hereafter the visibility and separation of ray extensions, halos, ray patterns, and additional focal points.

By applying the light sheet-based method the selected image area is accumulated line by line without considering the rotationally symmetric shape of the 3D-PSF of the investigated MIOL. Consequently, with increasing t the fine structures are overlapped by the accumulated intensity, further the background signal intensity from outer regions of the 3D-PSF increases, which all result in a lack of fine structure visibility.

To ensure comparability with documented CSIs acquired with fluorescein baths, the width $t = 43\,\mu m$ is used for calculating the CSIs of the light sheet-based method in the following. Moreover, the trimming and linear stretching of the lateral image area perpendicular to the axial position of the CSIs to three times of the original width is maintained.

3.2. Methods for image quality enhancement of 3D-PSF cross-sectional images

The optical bench allows the image recording of the 2D-PSFs and the corresponding background images for several axial positions, which each can be averaged over multiple exposures for an improved SNR. The influence of averaging and background signal correction was studied using the investigations of the aperture configuration $d_A = 3$ mm. An image stack with six images and six background images for each axial position was captured. For 4(a), only the first image per position was used. For 4(b), the first background image was subtracted. For 4(c), the six 2D-PSF images and six background images were each subtracted and averaged from each other. The corresponding cross-sectional images were calculated using the light sheet-based method. For 4(d), the averaged and subtracted images were evaluated with the new algorithm. The respective CSIs are shown in linearly scaled intensities in Fig. 4(a)-(d) and logarithmically scaled intensities in Fig. 4(e)-(h). In each CSI, the near focus is located at an axial position of ≈ 0.3 mm, the intermediate focus at ≈ 0.9 mm and the far focus at ≈ 1.35 mm. A clear separation of the near and intermediate focus can be seen. Further, low-intensity ray extensions are seen focusing and defocusing to various point positions along the optical axis. At the various focal points, especially at the intermediate focus, halos appear in the outer image areas.

The comparison of three CSIs presented in Fig. 4(a)-(c) shows no differences in shape, contrast, or intensity. Moreover, intensity is clearly visible in the defocus zone between the intermediate and far focus. Consequently, the exact separation of these two focal points is not possible. The influence of the background correction and the averaging is not visible in the linear illustration but becomes apparent in the logarithmically scaled intensities comparing Fig. 4(e)-(g). The background signal is emphasized by comparing Fig. 4(e) and Fig. 4(f) and looks like a gray shroud lying over the CSI. The influence of averaging is not as obvious as the background correction but becomes visible comparing the gray values in the outer image areas in the logarithmically scaled illustrations (see Fig. 4(f) and Fig. 4(g)). For the case of background correction and averaging, the rotationally averaged cross-sectional image (RA-CSI) was also calculated (see Fig. 4(d)). Fig. 4(d) shows clearly the three focal areas in the linear scaled RA-CSI of the new method are clearly separable (see Fig. 4(d)). Unlike the CSI of the light sheet-based method, there is no intensity in the defocus regions along the optical axis. The ray extensions at the outer focal areas can be seen in the linear illustration but are less prominent as in the light sheet-based method. In addition, some fine features can not be seen in the outer image areas like in Fig. 4(c) and 4(g) e.g. at 0.8 mm and near the lateral edges. Comparing the logarithmically scaled representations (see Fig. 4(e) - 4(h)), only the CSI of the new method reveals the three distinct focal points. Further,
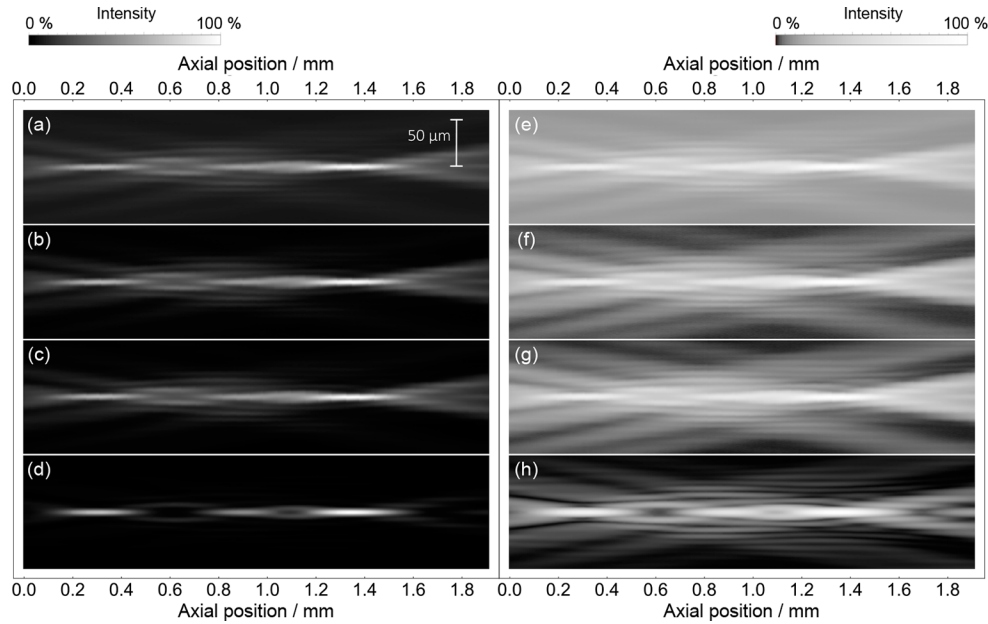
Fig. 4. CSIs determined from different image stacks captured with $d_{IOL} = 2.93$ mm: (a), (e) one captured picture for each axial position without background signal corrected and (b), (f) - with background signal corrected, (c), (g) six times averaged and background signal corrected, all calculated with the light sheet-based method with the width $t = 43$ μm, and (d), (h) averaged, and background signal corrected, and calculated using the new algorithm. The CSIs were each normalized to the maximum gray level of the four CSIs shown and are thus directly comparable. Further, these are shown in intensity-dependent gray values linearly and in logarithmically scaled intensities in the left and right column, respectively. The near focus is at the axial position of ≈ 0.3 mm, the intermediate focus at ≈ 0.9 mm and the far focus at ≈ 1.35 mm.

the individual ray pattern and halos are most evident in Fig. 4(g). It is worth noting that Fig. 4(g) reveals another focal point at an axial position of 1.9 mm. However, this has no relevance from the patient's point of view since this position lies behind the retina. The qualitative comparison of these illustrations shows that CSIs of the new method demonstrates a better fine feature visibility.

The signal-to-noise ratio (SNR) is an important and widely used quantity to study the influence of the different steps on the image quality improvement and is therefore also an important measurement to compare the quality of the captured signals. The axial positions of the focal points and the corresponding 2D-PSF images were determined by analyzing the intensity response along the optical axis and the respective 2D-PSF images of the different focal points extracted from the different image stacks and investigation methods (light sheet-based and new). The SNR values were calculated for the focal point images using the Eq. 2. For each of the four CSIs shown in Fig. 4, the respective SNR was calculated using Eq. 2 and the previously calculated largest values for A_S, σ_N, and A_N of the 2D-PSF images associated with a CSI.

Table 1 presents the calculated SNR values. The comparison reveals, that the background correction increases the SNR values of the single images of focal points by ≈ 26 % and of the CSI by ≈ 33 %. The image averaging increases the SNR of the single pictures on average by a factor ≈ 2.30 and for the CSI by a factor ≈ 2.49. With the new algorithm, the SNRs of the RA-CSIs and the images of the focal points are increased by roughly two orders of magnitude. Both Fig. 4 and the SNR-values show the impact of the new algorithm on the improvement of the image quality and the fine feature visibility. The newly developed method may give a deeper insight into the

experimental image formation. To study this in more detail, we use the light sheet-based and the newly developed method to calculate CSIs and RA-CSIs of image stacks captured with different pupil sizes hereinafter.

Table 1. The calculated SNR values of the CSIs shown in Fig. 4 by using Eq. (2). Further, the SNR of the image of the near, intermediate, and far focus, respectively, were calculated for the different combinations of the methods (light sheet-based and new annulus integration), averaging (AV), and background correction (BG).

Specification			SNR			
Method	BG	AV	Near	Intermediate	Far	CSI
Light sheet-based	-	-	616	349	917	867
Light sheet-based	+	-	796	435	1144	1130
Light sheet-based	+	+	1906	811	3013	2810
Annulus integration	+	+	214 000	99 600	318 000	222 000

3.3. Cross-sectional images depending on the illuminated intraocular lens diameter

The previous chapter showed that the new method for determining the cross-sectional images results in improved image quality. To obtain a deeper understanding of the image formation of the investigated MIOL and to compare the two methods for determining the CSIs in more detail, we study the CSIs depending on the illuminated IOL-diameter d_{IOL} ranging from 2.44 mm to 5.87 mm in 0.49 mm steps, according to 2.5 mm to 6.0 mm using Eq. (1). The proprietary algorithm was used for data processing and for determining the CSIs.

Fig. 5 shows the cross-sectional images calculated with the light sheet-based (left column) and the newly developed method (right column) for several illuminated IOL-diameters d_{IOL} in logarithmically scaled intensities. The CSIs of each column were normalized to the maximum gray level. The position of the near focus is at an axial position of ≈ 0.3 - 0.4 mm, of the intermediate focus at ≈ 0.9 mm and of the far focus between ≈ 1.35 - 1.55 mm. In each of the CSIs of both methods, the near focus is clearly separated in contrast to intermediate and far focus. For d_{IOL} of 2.44 mm, the intermediate and far focus overlap. As the d_{IOL} increases, the intermediate and far focus become increasingly separated.

For $d_{IOL} \geq 4.4$ mm, the defocus zone of intermediate and far focus (axial position = $1.0 - 1.2$ mm) shows the appearance of an additional focal point with very weak intensity, which becomes clearly visible with increasing d_{IOL}. In addition for $d_{IOL} \geq 4.89$ mm, a smearing of the three main focal points towards higher values of axial distances is observed. Other details that become visible only in the RA-CSI at d_{IOL} 5.38 mm and 5.87 mm are occurring interference effects along the individual ray extensions and halos in the outer image areas starting from the optical axis.

The comparison with the CSIs of the light sheet-based method (see the left column in Fig. 5) shows that all the observed extra focal points along the optical axis in the RA-CSIs of the new method are not detectable in these CSIs. The smearing of the focal points and the separation of the halos, however, is noticeable to some extent. In the RA-CSIs of the new method (see the right column in Fig. 5.) an additional focal point is visible at 1.9 mm for d_{IOL} from 2.93 mm to 3.91 mm. For larger pupil diameters, this one may shift to axial positions outside the image area shown. The observed additional focal points may be traced back to higher diffraction orders because of the diffractive character of the investigated IOL [14,40]. Due to their low intensity, these are overlaid by off-axis intensities due to the thickness of the virtual light sheet in the light sheet-based method.

To investigate the distribution of intensity along the optical axis in more detail, the through-focus curves were determined for the illuminated diameters 2.93 mm, 4.40 mm, and 5.87 mm by
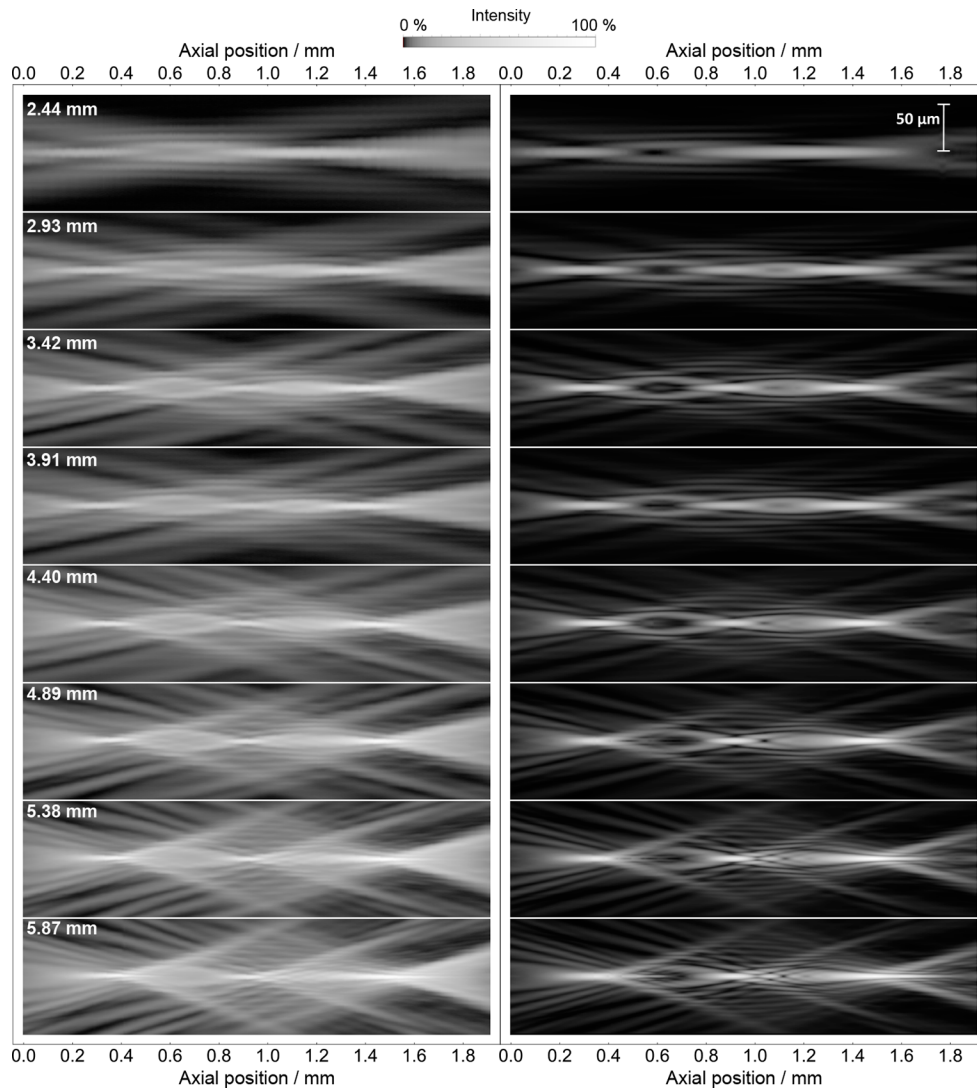
Fig. 5. Cross-sectional images calculated (left) with the light sheet-based and (right) the newly developed method depending on the illuminated IOL-diameter d_{IOL} (denoted in the upper left corner of each row) in logarithmically scaled intensity-depended gray values. The near focus is at the axial position of $\approx 0.3\,\mathrm{mm}$ - $0.4\,\mathrm{mm}$, the intermediate focus at $\approx 0.9\,\mathrm{mm}$ and the far focus at ≈ 1.35 - $1.45\,\mathrm{mm}$.

calculating the mean intensity of an 11×11 pixel centered to the optical axis for each captured image.

Fig. 6 shows the through-focus curve of $d_{\mathrm{IOL}} = 2.93\,\mathrm{mm}$ illustrated as —●—, $d_{\mathrm{IOL}} = 4.40\,\mathrm{mm}$ as —▲—, and $d_{\mathrm{IOL}} = 5.87\,\mathrm{mm}$ as —■—. The near focus is located in the axial position range between $0.3\,\mathrm{mm}$ and $0.4\,\mathrm{mm}$, the intermediate focus at $\approx 0.9\,\mathrm{mm}$, and the far focus between $1.35\,\mathrm{mm}$ and $1.55\,\mathrm{mm}$. With increasing pupil size, the intensity in the focal points increases, and the additional peaks, as seen in Fig. 5, between the axial distance of 1.0 - $1.2\,\mathrm{mm}$ become visible. Interestingly, for $d_{\mathrm{IOL}} = 5.87\,\mathrm{mm}$, a shoulder appears on the right side of the near- and far focus, which is most likely due to underlying peaks from a higher diffraction order. Additionally, the position of the near and the far focus shift to higher axial positions with increasing pupil sizes.
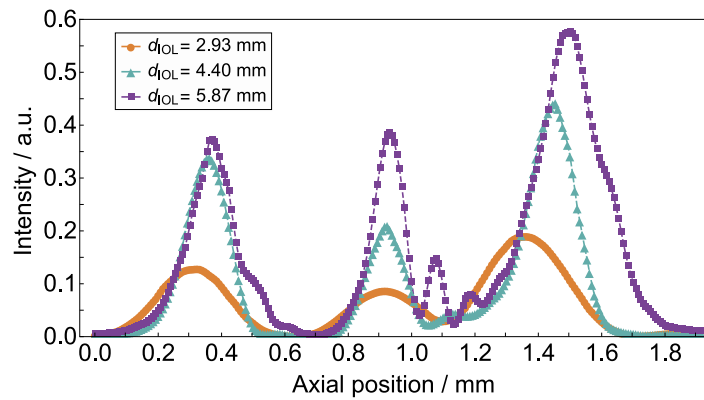
Fig. 6. Through-focus response as a function of the axial position for the illuminated IOL-diameters d_{IOL} 2.93 mm, 4.40 mm, and 5.87 mm.

4. Discussion

Our study has shown that the implementation of the new proprietary algorithm exploiting the rotational symmetry of IOLs has the advantage of image quality improvement of the corresponding cross-sectional images compared to the light sheet-based method. With regard to the light sheet-based method, we found that the smaller the thickness of the virtual light sheet the better image quality and fine feature visibility of the illustration of the cross-sectional images is.

Petelczyc et al. [17] reported a projection cross-sectional image of the AT LISA tri 839MP (Carl Zeiss Meditec AG, Jena, Germany) for a pupil size $d_A = 3$ mm, which is consistent with our findings and shows similarities in the distance between the focal points, higher gray values in the defocus zone between intermediate and far focus. Due to its different aspect ratio, halos and ray extensions are not as obvious as in the CSIs presented in Fig. 3. The greater SNR-values of the newly developed method are an indicator for image quality improvement.

The comparison of the CSIs quality and the SNR-values of the light sheet-based and the newly developed method clearly shows that an improvement of the CSI image quality and the fine feature visibility is achieved fulfilled by the newly developed algorithm. Furthermore, the individual fine structures like high diffraction orders, which have to be present in the case of a diffractive IOL, are clearly visible in a CSI for the first time. Accordingly, the extra focal points occurring between the intermediate and the far focus for $d_{IOL} \geq 4.4$ mm raise two questions that could be the subject of future experimental investigations and clinical trials. Do these focal points improve the visual acuity in the intermediate and far distance? Accordingly, does the investigated IOL have an EDOF-character (Extended Depth of Focus [42]) in the range of the intermediate to the distant focus for $d_{IOL} \geq 4.4$ mm?

We observed an overlap between the intermediate and far focus in the CSIs and the RA-CSIs for $d_A = 2.5$ mm. Consistent with our findings Vega et al. [43] reported that, based on the depth of field of a gaussian beam, the smaller the entrance pupil the longer the extension of the focus spot along the optical axis is, which lead to overlap between different focal point areas of MIOLs. In general, the calculation of the modulation transfer function (MTF) is often preferred, which is the quantity is the squared magnitude of the PSF, and easily and quickly accessible due to the fast Fourier transform [26]. Ruiz-Alcocer et al. investigated pupil size dependent through-focus modulation transfer function of the same IOL under investigation [44]. In accordance with our results, they observed only a peak for the near and far focus without an intermediate peak for $d_A < 3.0$ mm. Consequently, the overlapping of the intermediate- and far focus is due to the properties of the studied IOL.

In contrast to the newly developed method, the beam profiles of the light sheet-based methods show a very intense ray pattern even apart from the optical axis [17,19–21]. However, comparing to the newly developed method, which does not exhibit all of these off-axis light features, it evidently shows that methods based on light sheets of certain width give potentially misleading or even wrong results. Further, with our method we find an additional focal point behind the far focus, which may be attributed to a diffraction order of opposite sign compared to the diffraction orders of intermediate and near focus.

In the case of applying a fluorescein bath or an optical bench for the light sheet-based method, three critical thoughts should be mentioned. Firstly, the wider the light sheet, the more intensity is included from the image regions laterally distant from the optical axis, resulting in deviating cross-sectional images. Based on the fact that in the case of the fluorescein bath the beam profile is recorded by a side-mounted camera that captures an image averaged over the illuminated light sheet width, increasing the width of the illuminated light sheet would not result in any improvement in image quality. Secondly, it must be taken into account that fluorescence is based on a preceding absorption and hence the intensity along the optical axis may decrease. Stating this, it is not possible to guarantee, that a through-focus curve obtained from this method describes the intensity distribution along the optical axis correctly. This fact has not been studied till now. Thirdly, the image quality is usually reduced due to image artifacts resulting from the scattering dust of the used particles [19,20]. These critical problems are avoided by the approach of an optical bench in combination with the new algorithm.

Furthermore, axial smearing of the focal points was observed for the RA-CSIs in Fig. 5. The investigated MIOL has a spherical aberration (SA) of -0.18 μm for a 6.0 mm eye pupil to partially compensate a part of the natural positive SA of the human eye [45]. The observed smearing along the optical axis towards larger values of the axial position implies that the interaction between the SA of the model cornea and the MIOL creates a negative SA.

The through-focus curves show like the previous RA-CSIs higher diffraction orders and further an obvious drifting of the near and far focus to larger values of the axial position. Thus, the smearing may also be caused by superpositions of the main focus with a peak of a higher diffraction order, which is important especially for large pupils. This should be investigated in further research projects. The proprietary algorithm was developed for rotationally symmetric IOLs like monofocal and most multifocal diffractive IOLs. In addition to these IOLs, other MIOL design approaches exist that are based e.g. on the light sword method [17] or the combination of different refractive elements [46]. Due to their consequently asymmetric 3D-PSF, the application of the new algorithm will produce inaccurate CSIs leading to misinterpretations and wrong conclusions about the investigated IOLs. Recent IOL-designs compensating the aberrations induced by imaging at the kappa angle [47] are not rotationally asymmetric, however, their 3D-PSF should be symmetric, if the model eye is appropriately rotated around the nodal point. Hence, such IOLs could be evaluated using the newly developed method.

A drawback of the new algorithm is the long calculation time of the algorithm $t_C \approx 40$ min. The time consuming part of the algorithm originated from the fourfold increased edge length of the images using cubic-spline interpolation (38 % of t_C) and the annulus integration method (48 % of t_C). Accordingly, each image is increased from 3088×2076 pixels to 12352×8304 pixels. The application of another software such as Python, e.g. using SciPy [48], Matlab (The MathWorks Inc., Massachusetts, USA), or more efficient image processing algorithms of Mathematica (The Wolfram Centre, Oxfordshire, United Kingdom) may reduce the high calculation time. Other approaches may also include the parallel evaluation of graphic cards using CUDA [49] or OpenCL [50].

However, CSIs are widely used to understand the functional principles of different IOLs. The combination of an optical bench and the newly developed evaluation method allows a precise determination of the cross-sectional images of rotationally symmetric IOLs.

5.   Conclusion

This work compares different post-processing approaches for improving the quality of CSIs of IOLs, which are tested exemplifying on own captured 3D-PSFs of the AT LISA tri 839MP (Carl Zeiss Meditec AG, Jena, Germany). Further CSIs of the investigated IOL are presented for eight different pupil diameters by using two different visualization methods, the light sheet-based and the newly developed method, which for the first time specifically exploits the rotational symmetry of most IOLs like the AT LISA tri 839MP (Carl Zeiss Meditec AG, Jena, Germany).

The comparative study showed the clear superiority of the newly developed method in terms of image quality and signal-to-noise ratios compared to the light sheet based method. In addition, fine structures of the investigated MIOL like higher diffraction orders become visible in the CSIs of the newly developed method. Moreover, the off-axis intensities, e.g. halos, are now distinguishable with higher contrast and therefore easy to identify compared to other methods. The new algorithm will allow a better understanding of the character of the real experimental image formation induced by IOLs, which was previously limited using the light-sheet based method due to technical restrictions.

It is subject to future research, to extend the newly developed method to the determination of important optical properties of IOLs such as energy efficiency, modulation transfer function, or longitudinal chromatic aberration.

Disclosures.   The authors declare no conflicts of interest.

Data availability.   Data underlying the results presented in this paper are not publicly available at this time but may be obtained from the authors upon reasonable request.

References

1. S. Modi, R. Lehmann, A. Maxwell, K. Solomon, R. Cionni, V. Thompson, J. Horn, M. Caplan, B. Fisher, J. G. Hu, and E. Yeu, "Visual and patient-reported outcomes of a diffractive trifocal intraocular lens compared with those of a monofocal intraocular lens," Ophthalmology **128**(2), 197–207 (2021).
2. J. A. Davison and M. J. Simpson, "History and development of the apodized diffractive intraocular lens," J. Cataract Refractive Surg. **32**(5), 849–858 (2006).
3. G. Auffarth, T. Rabsilber, T. Kohnen, and M. Holzer, "Design and optical principles of multifocal lenses," Ophthalmologe **105**(6), 522–526 (2008).
4. L. C. Salerno, M. C. Tiveron, and J. L. Alió, "Multifocal intraocular lenses: types, outcomes, complications and how to solve them," Taiwan J. Ophthalmol. **7**(4), 179 (2017).
5. V. Maurino, B. D. Allan, G. S. Rubin, C. Bunce, W. Xing, and O. Findl, "Quality of vision after bilateral multifocal intraocular lens implantation," Ophthalmology **122**(4), 700–710 (2015).
6. M. J. Simpson, "Diffractive multifocal intraocular lens image quality," Appl. Opt. **31**(19), 3621 (1992).
7. L. Carretero, C. González, A. Fimia, and I. Pascual, "Application of the ronchi test to intraocular lenses: A comparison of theoretical and measured results," Appl. Opt. **32**(22), 4132 (1993).
8. G. Bos, J.-M. Vanzo, J. Maufoy, and J. L. Gutzwiller, "New interferometric method to assess intraocular lens characteristics," Proc. SPIE **2127**, 56 (1994).
9. G. Ravalico, F. Parentin, P. Sirotti, and F. Baccara, "Analysis of light energy distribution by multifocal intraocular lenses through an experimental optical model," J. Cataract Refractive Surg. **24**(5), 647–652 (1998).
10. I. O. for Standardization, "ISO11979-2:2000-07 ophthalmic implants – intraocular lenses – part 2: optical properties and test methods," (2000).
11. E. Peli and A. Lang, "Appearance of images through a multifocal intraocular lens," J. Opt. Soc. Am. A **18**(2), 302 (2001).
12. F. Castignoles, M. Flury, and T. Lepine, "Comparison of the efficiency, MTF and chromatic properties of four diffractive bifocal intraocular lens designs," Opt. Express **18**(5), 5245 (2010).
13. T. Kawamorita and H. Uozato, "Modulation transfer function and pupil size in multifocal and monofocal intraocular lenses in vitro," J. Cataract Refractive Surg. **31**(12), 2379–2385 (2005).
14. W. Hill, D. Carson, X. Hong, and M. Karakelle, "Optical bench performance of AcrySof IQ ReSTOR, AT LISA tri, and FineVision intraocular lenses," Clin. Ophthalmol. **8**, 2105–2113 (2014).
15. S. Lee, M. Choi, Z. Xu, Z. Zhao, E. Alexander, and Y. Liu, "Optical bench performance of a novel trifocal intraocular lens compared with a multifocal intraocular lens," Clin. Ophthalmol. **10**, 1031–1038 (2016).

16. M. S. Millán and F. Vega, "Through-focus energy efficiency and longitudinal chromatic aberration of three presbyopia-correcting intraocular lenses," Trans. Vis. Sci. Tech. **9**(12), 13 (2020).
17. K. Petelczyc, A. Kolodziejczyk, N. Błocki, A. Byszewska, Z. Jaroszewicz, K. Kakarenko, K. Kołacz, M. Miler, A. Mira-Agudelo, W. Torres-Sepúlveda, and M. Rkekas, "Model of the light sword intraocular lens: in-vitro comparative studies," Biomed. Opt. Express **11**(1), 40 (2020).
18. S. Reiß, J. Forbrig, R. Guthoff, T. Terwee, H. Stolz, S. Siewert, A. El-Tamer, U. Hinze, B. Chichkov, and O. Stachs, "Optimisation of the visualisation technique for optical paths through intraocular lenses for characterisation of multifocal imaging properties of fresnel-zone plates," Klin. Monatsbl. Augenheilkd. **231**, 1183–1186 (2014).
19. H. Weeber, T. Terwee, M. van der Mooren, and P. Piers, "Visualization of the retinal image in an eye model with spherical and aspheric, diffractive, and refractive multifocal intraocular lenses," J. Cataract Refractive Surg. **24**(3), 223–232 (2008).
20. T. Eppig, K. Rubly, A. Rawer, and A. Langenbucher, "Visualization of light propagation with multifocal intraocular lenses using the ouzo effect," BioMed Res. Int. **2019**, 1–10 (2019).
21. H.-S. Son, G. Łabuz, R. Khoramnia, T. M. Yildirim, C. Y. Choi, M. C. Knorz, and G. U. Auffarth, "Visualization of forward light scatter in opacified intraocular lenses and straylight assessment," Diagnostics **11**(8), 1512 (2021).
22. U. Hinze, A. El-Tamer, L. L. Doskolovich, E. A. Bezus, S. Reiß, H. Stolz, R. F. Guthoff, O. Stachs, and B. Chichkov, "Additive manufacturing of a trifocal diffractive-refractive lens," Opt. Commun. **372**, 235–240 (2016).
23. H. S. Son, G. Labuz, R. Khoramnia, P. Merz, T. M. Yildirim, and G. U. Auffarth, "Ray propagation imaging and optical quality evaluation of different intraocular lens models," PLoS One **15**(5), e0233829 (2020).
24. H.-S. Son, G. Łabuz, R. Khoramnia, T. M. Yildirim, and G. U. Auffarth, "Laboratory analysis and ray visualization of diffractive optics with enhanced intermediate vision," BMC Ophthalmol. **21**(1), 197 (2021).
25. I. O. for Standardization, "ISO11979-2:2014-2 ophthalmic implants – intraocular lenses – part 2: Optical properties and test methods," (2014).
26. R. Rawer, W. Stork, C. W. Spraul, and C. Lingenfelder, "Imaging quality of intraocular lenses," J. Cataract Refractive Surg. **31**(8), 1618–1631 (2005).
27. F. Alba-Bueno, F. Vega, and M. S. Millán, "Design of a test bench for intraocular lens optical characterization," J. Phys.: Conf. Ser. **274**(1), 012105 (2011).
28. S. Wahl, C. Song, and A. Ohlendorf, "Comparison of two devices to simulate vision with intraocular lenses," Clin. Ophthalmol. **13**, 123–130 (2019).
29. M. Gerlach, R. Guthoff, O. Stachs, S. Bohn, and K. Sperlich, "Pre-clinical evaluation of intraocular lenses through simulated implantation," Klin Monatsbl Augenheilkd **235**, 1332–1341 (2018).
30. J. Pujol, M. Aldaba, A. Giner, J. Arasa, and S. O. Luque, "Visual performance evaluation of a new multifocal intraocular lens design before surgery," Invest Ophthalmol Vis Sci. **55**, 3752 (2014).
31. M. K. Cheezum, W. F. Walker, and W. H. Guilford, "Quantitative comparison of algorithms for tracking single fluorescent particles," Biophys. J. **81**(4), 2378–2388 (2001).
32. B. Shuang, J. Chen, L. Kisley, and C. F. Landes, "Troika of single particle tracking programing: SNR enhancement, particle identification, and mapping," Phys. Chem. Chem. Phys. **16**(2), 624–634 (2014).
33. A. B. Watson and J. I. Yellott, "A unified formula for light-adapted pupil size," J. Vis. **12**(10), 12 (2012).
34. K. Dumbleton, M. Guillon, P. Theodoratos, C. Wooley, and K. Moody, "The effect of age and refractive error on pupil size," Invest. Ophthalmol. Vis. Sci. **56**, 585 (2015).
35. I. S. IDS Imagaging Development Systems GmbH, "Emva1288-ui-3880cp-m-gl-r2-default-settings," (2017).
36. S. Hecht, "Intensity and the process of photoreception," J. Gen. Physiol. **2**(4), 337–347 (1920).
37. S. Pieh, B. Lackner, G. Hanselmayer, R. Zöhrer, M. Sticker, H. Weghaupt, A. Fercher, and C. Skorpik, "Halo size under distance and near conditions in refractive multifocal intraocular lenses," Br. J. Ophthalmol. **85**(7), 816–821 (2001).
38. F. Vega, F. Alba-Bueno, M. S. Millán, C. Varón, M. A. Gil, and J. A. Buil, "Halo and through-focus performance of four diffractive multifocal intraocular lenses," Invest. Ophthalmol. Visual Sci. **56**(6), 3967–3975 (2015).
39. M. Ramamurthy and V. Lakshminarayanan, "Human vision and perception," in *Handbook of Advanced Lighting Technology*, R. Karlicek, C.-C. Sun, G. Zissis, and R. Ma, eds. (Springer International Publishing, 2015).
40. D. Gatinel, C. Pagnoulle, Y. Houbrechts, and L. Gobin, "Design and qualification of a diffractive trifocal optical profile for intraocular lenses," J. Cataract Refractive Surg. **37**(11), 2060–2067 (2011).
41. J. A. Futhey, "Diffractive bifocal intraocular lens," Proc. SPIE **1052**, 142–149 (1989).
42. J. F. Zapata-Díaz, M. A. Rodríguez-Izquierdo, N. Ould-Amer, J. Lajara-Blesa, and N. López-Gil, "Total depth of focus of five premium multifocal intraocular lenses," J. Cataract Refractive Surg. **36**(9), 578–584 (2020).
43. F. Vega, F. Alba-Bueno, and M. S. Millán, "Energy efficiency of a new trifocal intraocular lens," J. Eur. Opt. Soc. Rapid Publ. **9**, 14002 (2014).
44. J. Ruiz-Alcocer, D. Madrid-Costa, S. García-Lázaro, T. Ferrer-Blasco, and R. Montés-Micó, "Optical performance of two new trifocal intraocular lenses: through-focus modulation transfer function and influence of pupil size," Clin. & Exp. Ophthalmol. **42**(3), 271–276 (2014).
45. J. F. Montin, "Achieving spectacle independence with the AT LISA tri 839mp," Cataract. & Refract. Surg. Today Eur. **3**, 1 (2012).

46. J. L. Alio, A. B. Plaza-Puche, J. Javaloy, M. J. Ayala, L. J. Moreno, and D. P. Piñero, "Comparison of a new refractive multifocal intraocular lens with an inferior segmental near add and a diffractive multifocal intraocular lens," Ophthalmology **119**(3), 555–563 (2012).

47. B. Chassagne and L. Canioni, "Analytical solution of a personalized intraocular lens design for the correction of spherical aberration and coma of a pseudophakic eye," Biomed. Opt. Express **11**(2), 850 (2020).

48. P. Virtanen, R. Gommers, T. E. Oliphant, M. Haberland, T. Reddy, D. Cournapeau, E. Burovski, P. Peterson, W. Weckesser, J. Bright, S. J. van der Walt, M. Brett, J. Wilson, K. J. Millman, N. Mayorov, A. R. J. Nelson, E. Jones, R. Kern, E. Larson, C. J. Carey, İ. Polat, Y. Feng, E. W. Moore, J. VanderPlas, D. Laxalde, J. Perktold, R. Cimrman, I. Henriksen, E. A. Quintero, C. R. Harris, A. M. Archibald, A. H. Ribeiro, F. Pedregosa, and P. van Mulbregt, "SciPy 1.0: fundamental algorithms for scientific computing in Python," Nat. Methods **17**(3), 261–272 (2020).

49. NVIDIA, P. Vingelmann and F. H. Fitzek, "Cuda, release: 10.2.89," (2020).

50. G. Bradski, "The OpenCV Library," Dr. Dobb's J. Softw. Tools (2000).